Supplementary Information

Crystal reconstructed Cubic Nickel Oxide with Energetic Reactive Interfaces for Exceptional Electrochromic Smart Window

Chengyv Hu†, Xiaodan Guo†, Yi Gao, Ping Zhang, Pengyang Lei, Ying Lv, Xinyi Wang, Rui Zhu*, Guofa Cai*

Key Laboratory for Special Functional Materials of Ministry of Education, National & Local Joint Engineering Research Center for High-efficiency Display and Lighting Technology, and School of Nanoscience and Materials Engineering, Henan University, Kaifeng 475004, China.

† These authors have contributed equally to this work: Chengyv Hu, Xiaodan Guo

E-mail: zhurui@henu.edu.cn (Rui Zhu); caiguofa@henu.edu.cn (Guofa Cai)

This file includes:

Methods.

Supplementary Figures 1-16.

Supplementary Tables 1-2.

Supplementary References.

Methods

Materials. Nickel sulfate hexahydrate (NiSO$_4$·6 H$_2$O, ≥98%) was purchased from Sinopharm Chemical Reagents. Sodium hypophosphite monohydrate (NaH$_2$PO$_2$·H$_2$O, ≥99%) and potassium persulfate (K$_2$S$_2$O$_8$, ≥99%) were purchased from Aladdin Industrial Corporation. Potassium hydroxide (KOH, 85%) and Ammonia liquor (NH$_3$·H$_2$O, 28%) were purchased from Kermel Chemical Reagent. Deionized water is prepared in a water purifier (Milli-Q 18 MΩ, Millipore Corp). None of the reagents were further purified. Fluorine-doped tin oxide (FTO)-coated transparent conductive glass with a sheet resistance of 7 Ω sq^{-1} and transmittance of 80% was purchased from Guluo Glass Co., Ltd.

Preparation of Ni(OH)$_2$ nanosheet films. Ni(OH)$_2$ nanosheet films were synthesized by the chemical bath deposition method according to previous reports.[1] Typically, NiSO$_4$·6H$_2$O (13.14 g) and K$_2$S$_2$O$_8$ (4.054 g) were dissolved into 230 ml of deionized water and stirred for 15 min. Meanwhile, fix the FTO (50 × 20 mm) on the inner wall of a 300 ml beaker. After that, transfer 20 ml of ammonia and the above solution to the beaker with FTO, and stir for 15 min. After the reaction, the film was rinsed thoroughly with deionized water and then dried at 60 °C for 12 h.

Preparation of phosphorylated P-NiO and unphosphorylated NiO films. P-NiO films were obtained by chemical vapor deposition method. Firstly, the Ni(OH)$_2$ film was transferred into a tube furnace and heated at 300 °C under an air atmosphere for 60 min. Then, the NaH$_2$PO$_2$·H$_2$O was put at the upper end of the films and heated at 250 °C for 60 min under the Ar atmosphere. In addition, the unphosphorylated NiO nanosheet film was prepared under the same conditions without the participation of the NaH$_2$PO$_2$·H$_2$O for comparison.

Preparation of the 1 M KOH and activation of carbon paper. The electrolyte was prepared by dissolving 0.56 g KOH into the 10 ml deionized H$_2$O and then stirring for 15 min. The carbon paper was cut into a 4 × 4 cm^2 loop and then treated in 1 M H$_2$SO$_4$ for 10 min at 2.7 V by the three−electrode method to activate. Specifically, carbon paper was used as the working electrode, graphite was used as the counter electrode and Ag/AgCl was used as the reference electrode.

Assembly of device. The device was composed of P-NiO as an electrochromic layer, activated carbon paper as an ion storage layer and 1 M KOH as an electrolyte. Firstly, the carbon paper was fixed to the FTO glass to support it. Then, 3 M tape with a thickness of 1.5 mm was used to connect the P-NiO layer and the carbon paper layer and guarantee sufficient space for the electrolyte. Finally, the P-NiO electrochromic device was obtained by injecting the electrolytes into the void and sealing them with epoxy resin.

Materials characterization. X-ray diffraction (XRD, D8-ADVANCE) was performed to analyze the composition and crystal structure of the material. The microstructure, crystal plane parameters and elements distribution were characterized by field emission scanning electron microscopy (FESEM, Navo NanoSEM 450) and transmission electron microscopy (TEM, JEM-2100). Infrared spectral data of the film was obtained by the Frontier IR/FIR STA 8000 spectrometer (PerkinElmer, USA) with an attenuated total reflection detector in the 400 to 4000 cm^{-1} range. To determine the elemental composition and valence of electrochromic films, X-ray photoelectron spectroscopy (XPS) was performed by AXIS ULTRA X-ray photoelectron spectrometer. In addition, the elemental content of the P-NiO films at different depths was measured by argon ion etching. The Brunauer-Emmett-Teller (BET, Micromeritics ASAP 2460) measurement was conducted to analyze pore structure of P-NiO powder.

Electrochemical and electrochromic characterization. The electrochromic and electrochemical performances of the film were characterized by the three-electrode system test with the aqueous solution containing 1 M KOH as the electrolyte, the film as the working electrode, the Pt line as the counter electrode, and the Ag^+/Ag as the reference electrode. Cyclic voltammetry (CV) and square wave potential were performed on the Autolab Electrochemical Workstation (PGSTAT 302 N). The spectra of the film and device were measured by Shimadzu UV-3600 Plus spectrophotometer, using blank FTO and air as the baseline, respectively. The in situ spectra of the film were obtained by combining the electrochemical workstation and spectrophotometer.

Calculation details. The ab-initio molecular dynamics method and supercell models are employed to study the adsorption properties. A $2 \times 2 \times 2$ cubic NiO supercell was used, considering XRD results. And $2 \times 1 \times 1$ supercell orthorhombic $Ni_4P_2O_9$, where the content of P is relatively low, serves as the initial configuration. The (111) NiO surface and (001) $Ni_4P_2O_9$ surface were constructed through a slab model, and a 20 Å vacuum region was added. Based on the experiment process, 1 M KOH aqueous solution was used as the electrolyte, where a=12.00 Å, b=12.00 Å, and c=5.00 Å crystal containing a KOH molecule. To obtain the solution structure, canonical ensemble (NVT) simulation of KOH aqueous solution with a Nosé-Hoover thermostat at temperature 300 K. Abutment of KOH solution and electrochromic layer with different height have been optimized, and 3000 step NVT simulation as KOH aqueous solution. Then, the structure of the latest NVT results was used to do 3000 step micro-canonical ensemble simulation. The calculations were carried out with the GGA-PBE[2] functional on CP2K software.[3, 4] DZVP-MOLOPT-SR-GTH basis sets and Goedecker-Teter-Hutter (GTH) pseudopotentials were employed.[5, 6] The vdw-DF3 functional for the exchange correlation was

employed, because van der Waals interactions play a major role in the stability of the interface.[7, 8] The valence wave functions were expanded by plane waves with a cutoff energy of 400 eV. The MD was executed by at temperature 300 K, where a time step is 1 fs.[9]

The calculation method of $T_{lum, sol}$:

$$T_{vis, sol}=\int\varphi_{vis, sol}(\lambda)T(\lambda)d\lambda/\int\varphi_{vis, sol}(\lambda)d\lambda$$

Where $T(\lambda)$ represents the transmittance at wavelength λ, φlum (λ) denotes the standard efficiency function for photopic vision, and φsol (λ) is the solar irradiance spectrum for an air mass of 1.5, which corresponds to the sun standing at 37° above the horizon. The variation in transmittance at different potential (A) is defined as the solar modulation ability, $\Delta T_{sol}=T_{sol}$ (A)-T_{sol} (–0.3 V).

Energy saving performance simulation. The heating and cooling energy was modeled from the building energy simulation using EnergyPlus 8.7 and OpenStudio 2017 software. In particular, the building consists of a 15 m (L) × 10 m (W) × 3 m (H) house with a window-to-wall ratio of 1/3 (Fig. S16, SEI) and a 50 m (L) × 30 m (W) × 12 m house with a window-to-wall ratio of 1/4 (Fig. S17, SEI). The building's north axis is 0 degree to true north and the sill height is 0.76 m. The "ideal-loads-air-systems" were served by district cooling and heating sources. The thermostat setpoint is 24 °C cooling and 20 °C heating. The building energy saving performances are obtained by measuring the differences in values between the bleached/colored state of devices and clear 3mm glass specimen (baseline). The building surface details of the model are displayed in Supporting Information Table S2.

The CO_2 emission reductions in metric tons are converted from kilowatt-hours using the relevant factor as follows:

$$1 \text{ kWh} = 0.709 \text{ kg of } CO_2$$

The parallel experiments and micro-canonical ensemble simulation results

To further confirm the results, parallel tests with different original distances of electrolyte and electrochromic layer, and micro-canonical ensemble simulations were calculated (Fig. S11 to S13). We changed the position of K^+ in parallel experiment I and increased the distance between the KOH aqueous layer and the material to 5 Å in parallel experiment II.

In parallel experiment I on P-NiO, the OH^- and H_2O also adsorbed rapidly on the surface of P-NiO in the form of O-P during the NVT process. In parallel experiment II for P-NiO, only K^+ binds to OH^- and H_2O in the NVT process due to the large spacing system. In parallel experiments performed on NiO, OH^- was still adsorbed indirectly on NiO during the NVT process through the connection with K^+. In the NVE of parallel experiment I on P-NiO, OH^- stable adsorption is in the same position as NVT.

4

In the NVE of parallel experiment II on P-NiO, P demonstrated a rapid adsorption process for OH^- and H_2O. During the NVE process, OH^- reached the vicinity of K^+ by proton exchange and bound to K^+ and Ni, and then stabilized, proving the conclusion that the adsorption of OH^- on the surface of NiO is dependent on K^+. In parallel experiments performed on NiO, during the NVE process, OH^- reached the vicinity of K^+ by proton exchange and bound to K^+ and Ni, and then stabilized.

Overall, the results of the parallel experiments again demonstrated that the introduction of P provided new P-O adsorption sites, accelerated the OH^-–H_2O adsorption process, and freed OH^- adsorption from the dependence on K^+.
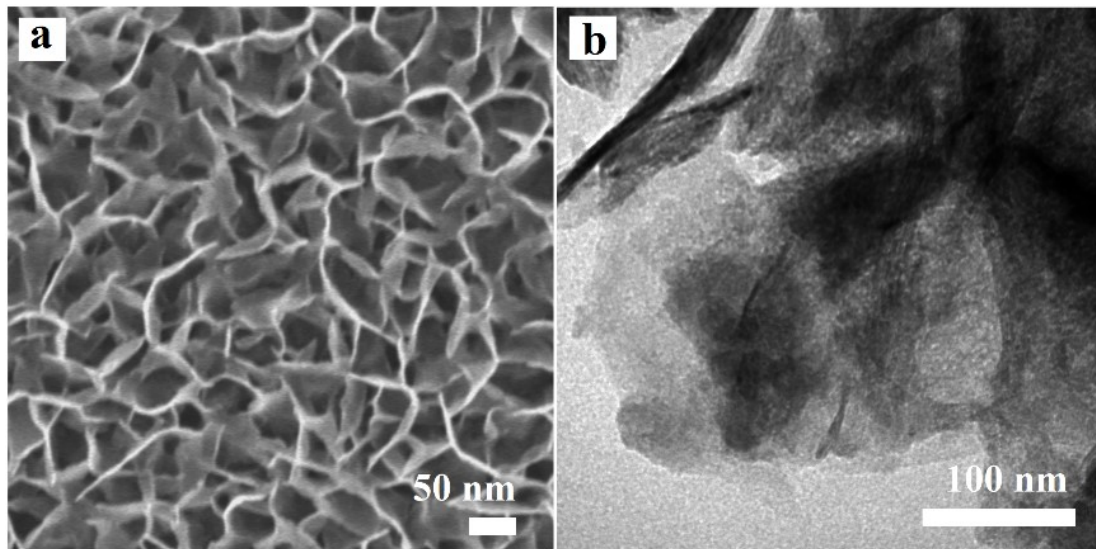
Fig. S1. a) SEM and b) TEM images of the NiO film.
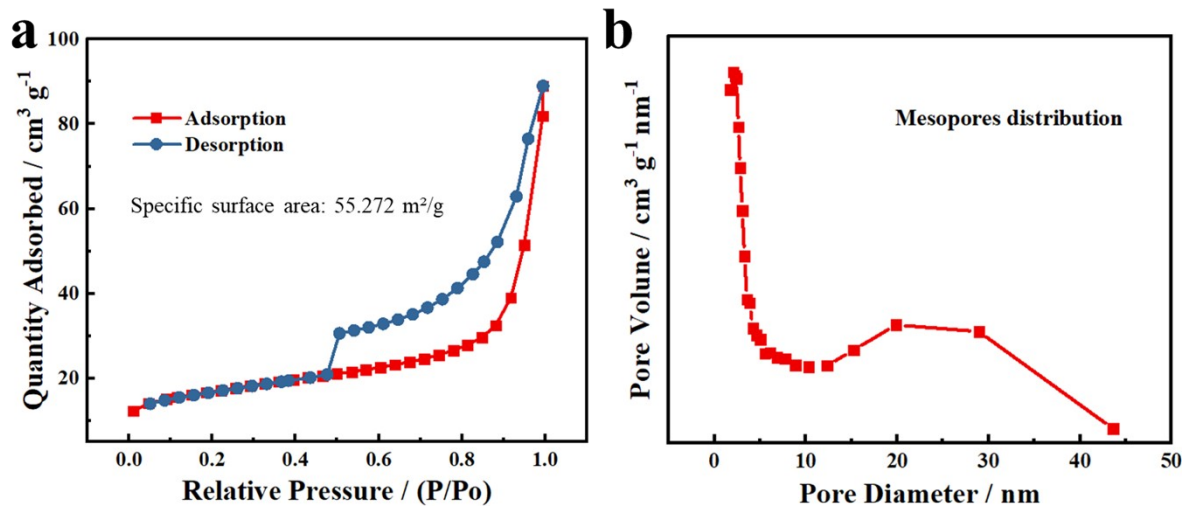
Fig. S2 a) N$_2$ isotherms at 77 K b) and the pore diameter distribution of the P–NiO.
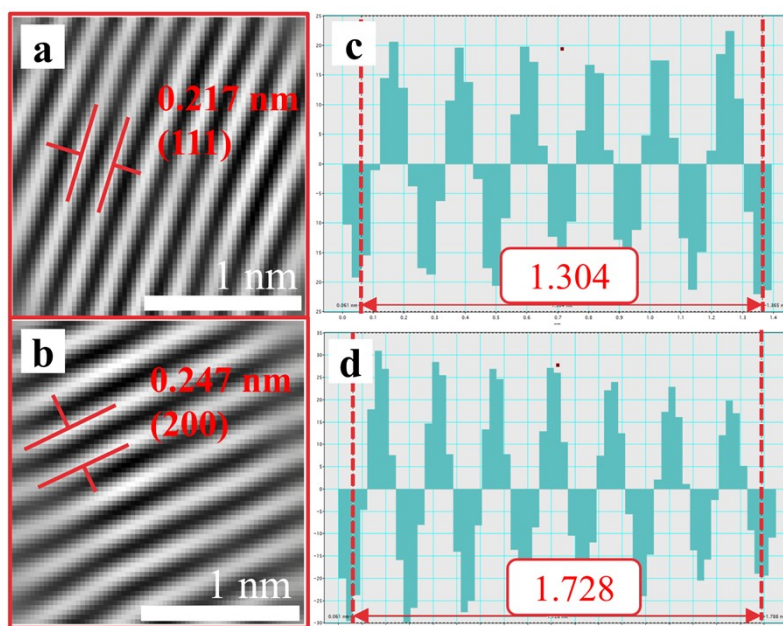
Fig. S3. TEM images of the P-NiO. a, b) Partial lattice stripes after refinement using Digital micrograph software. c, d) Calculations using Digital micrograph software to obtain the total length of multiple lattice spacings.
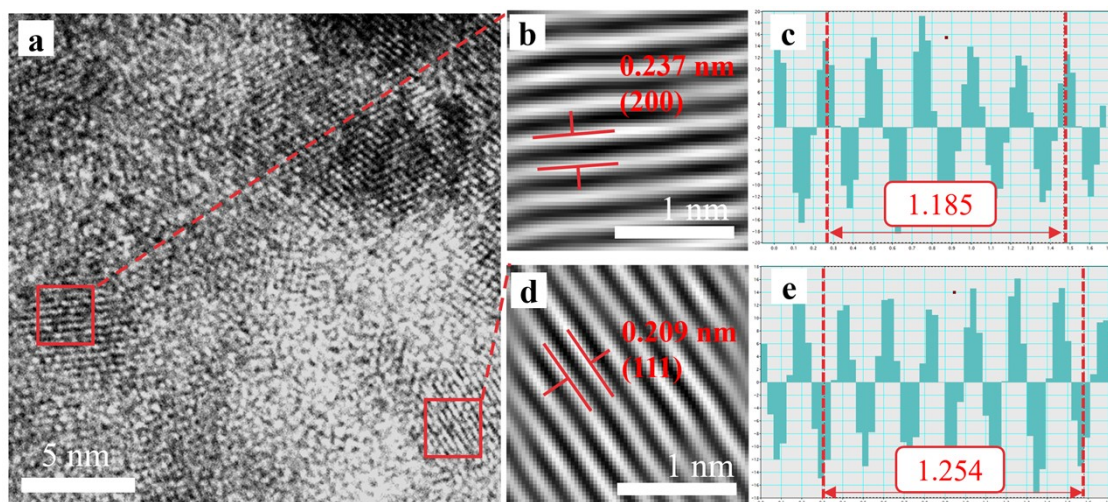
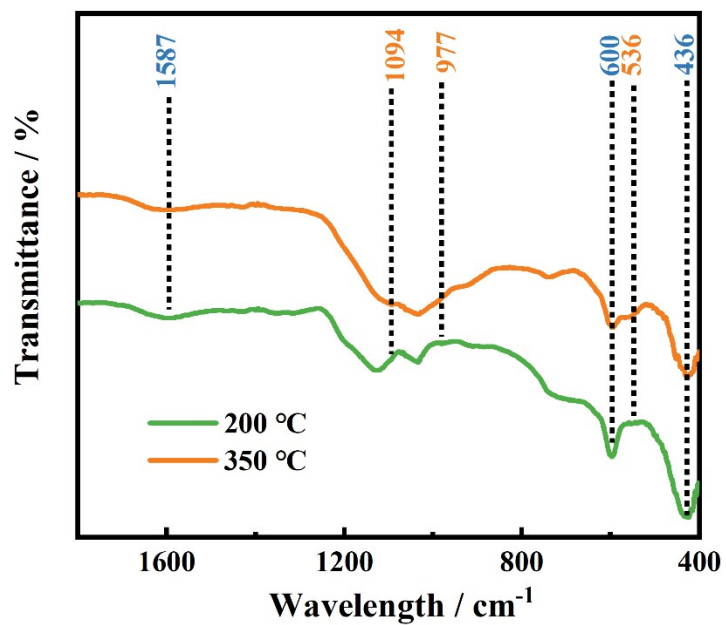**Fig. S4** a) TEM images of the NiO, b) and d) Partial lattice stripes after refinement using Digital micrograph software. c) and e) Calculations using Digital micrograph software to obtain the total length of multiple lattice spacings.

Fig. S5. FTIR results of P-NiO films on FTO substrate at different temperatures.
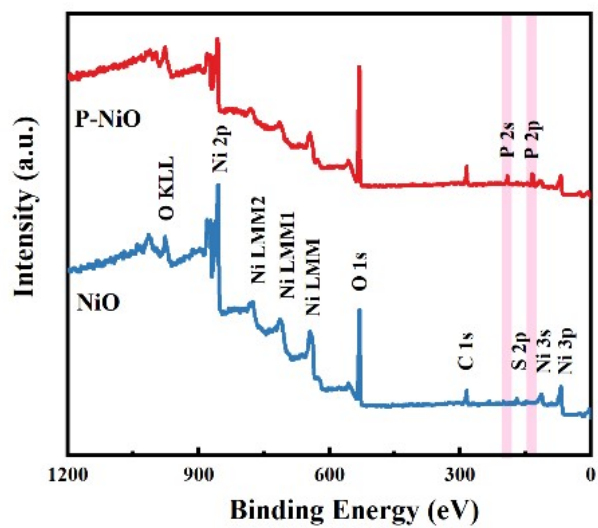
Fig. S6. XPS survey of P-NiO and NiO.
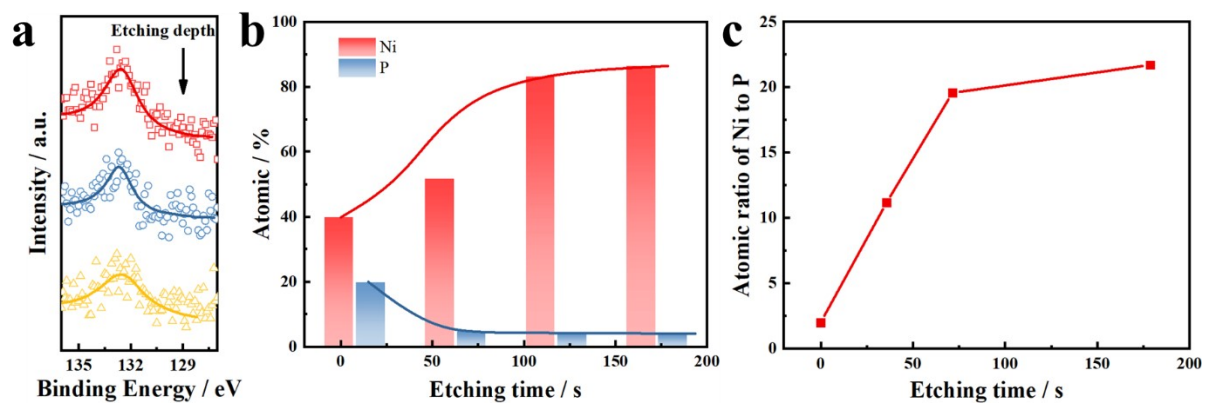
Fig. S7. a) High resolution spectrum of P 2p after etching. b) Atomic percentage of P and Ni. c) Atomic ratio of Ni to P at different etching times.
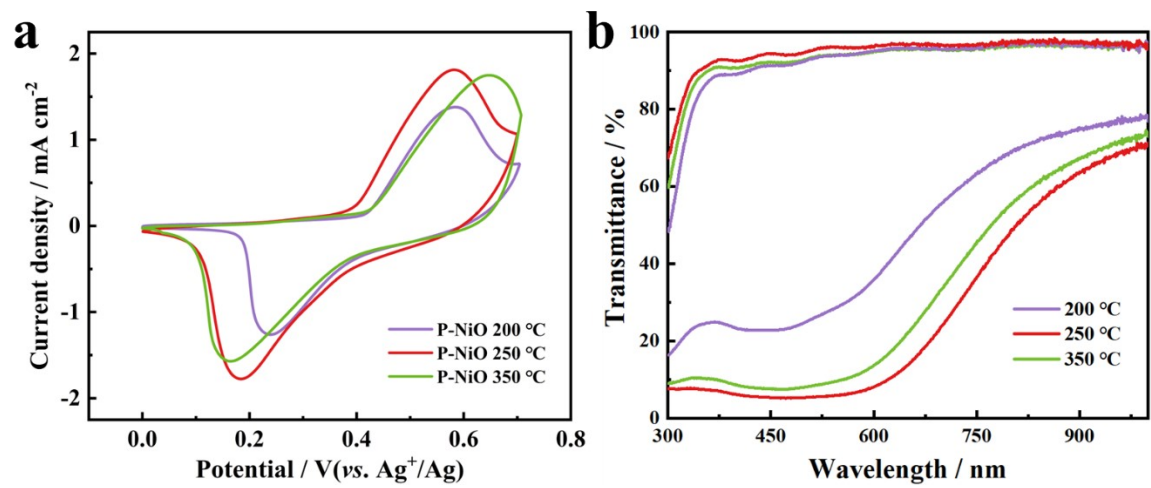
Fig. S8. a) CV curves and b) transmittance spectral at coloring and bleaching states of P-NiO films at different phosphorylation annealing temperatures.

13
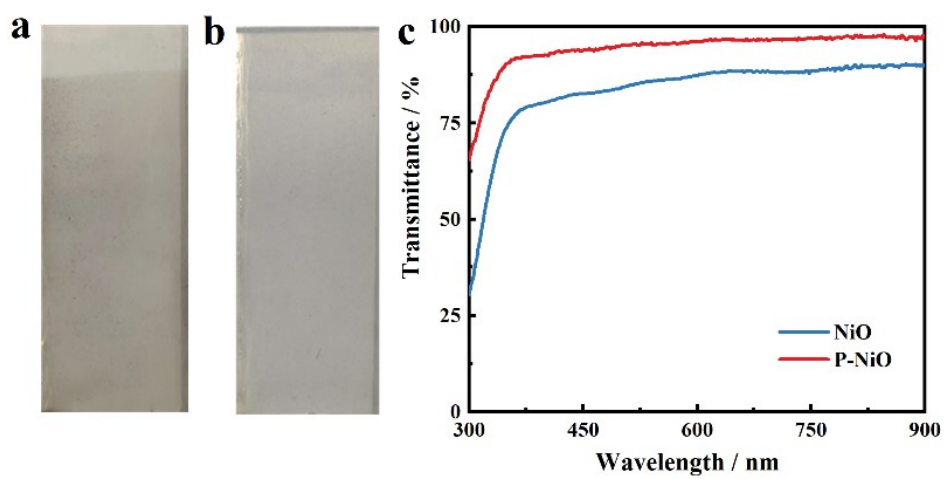
Fig. S9. a) NiO/FTO film. b) P-NiO/FTO film. c) Transmittance change from 300 nm to 900 nm in the initial state of P-NiO and NiO.
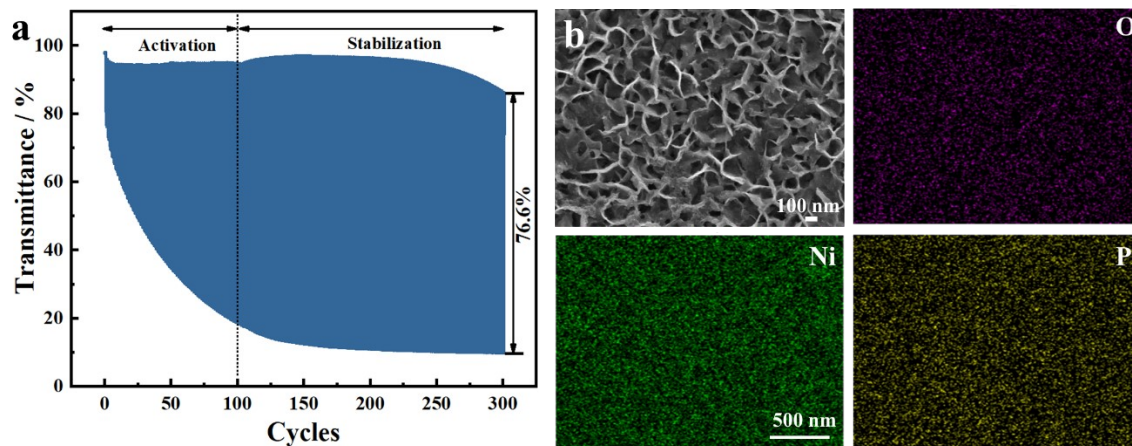
Fig. S10. a) In situ transmittance spectra of 300 cycles CA teat at 500 nm in the 0-0.7 V vs. Ag⁺/Ag windows (each 30 s). b) SEM and EDS images of the film after cyclic test.
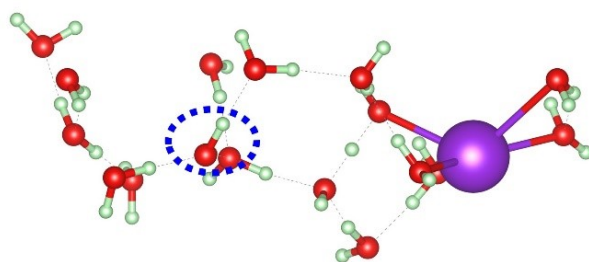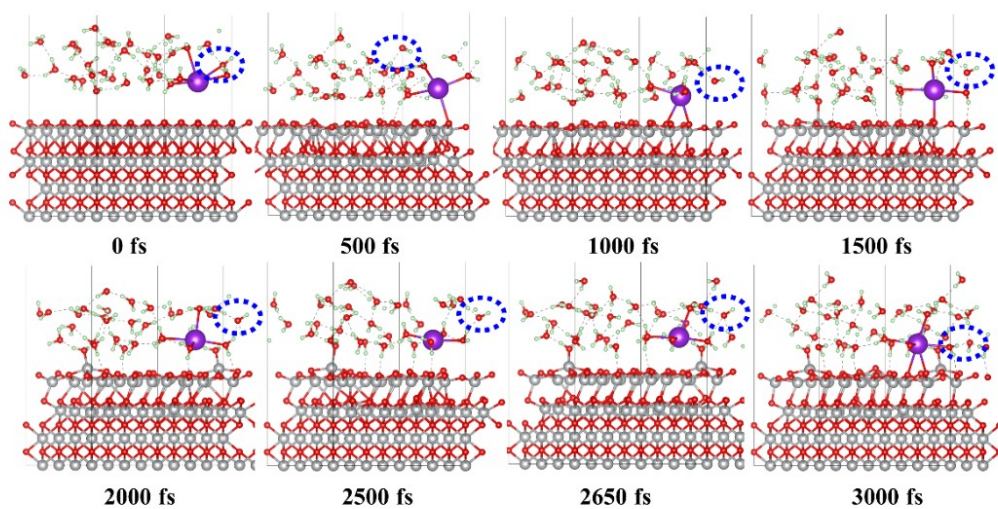
Fig. S11 The KOH/H$_2$O layer after NVT.

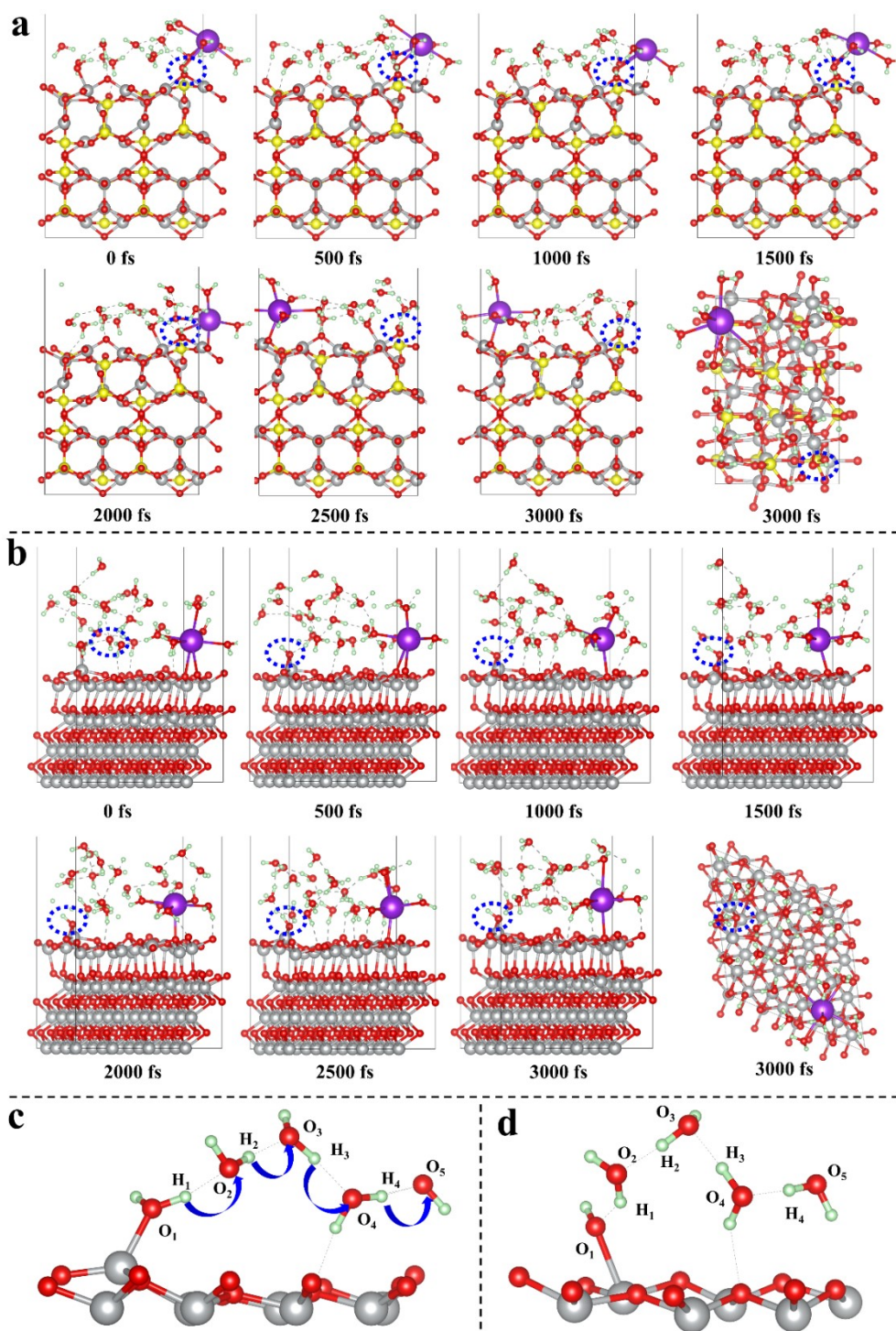**Fig. S12** NVT simulations of 1 M KOH adsorption on NiO.

Fig. S13 NVE simulations of a) P-NiO and b) NiO adsorption on 1 M KOH, schematic diagram of proton conversion before c) and after d).
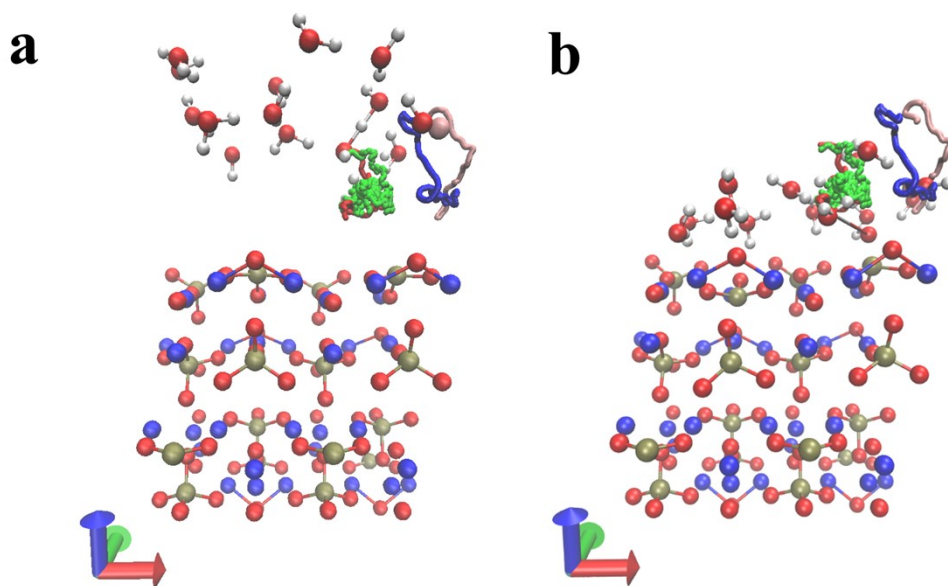
Fig. S14. Schematic trajectories of OH$^-$ and K$^+$ during. a) NVT and b) NVE of 1 M KOH adsorption on P-NiO.
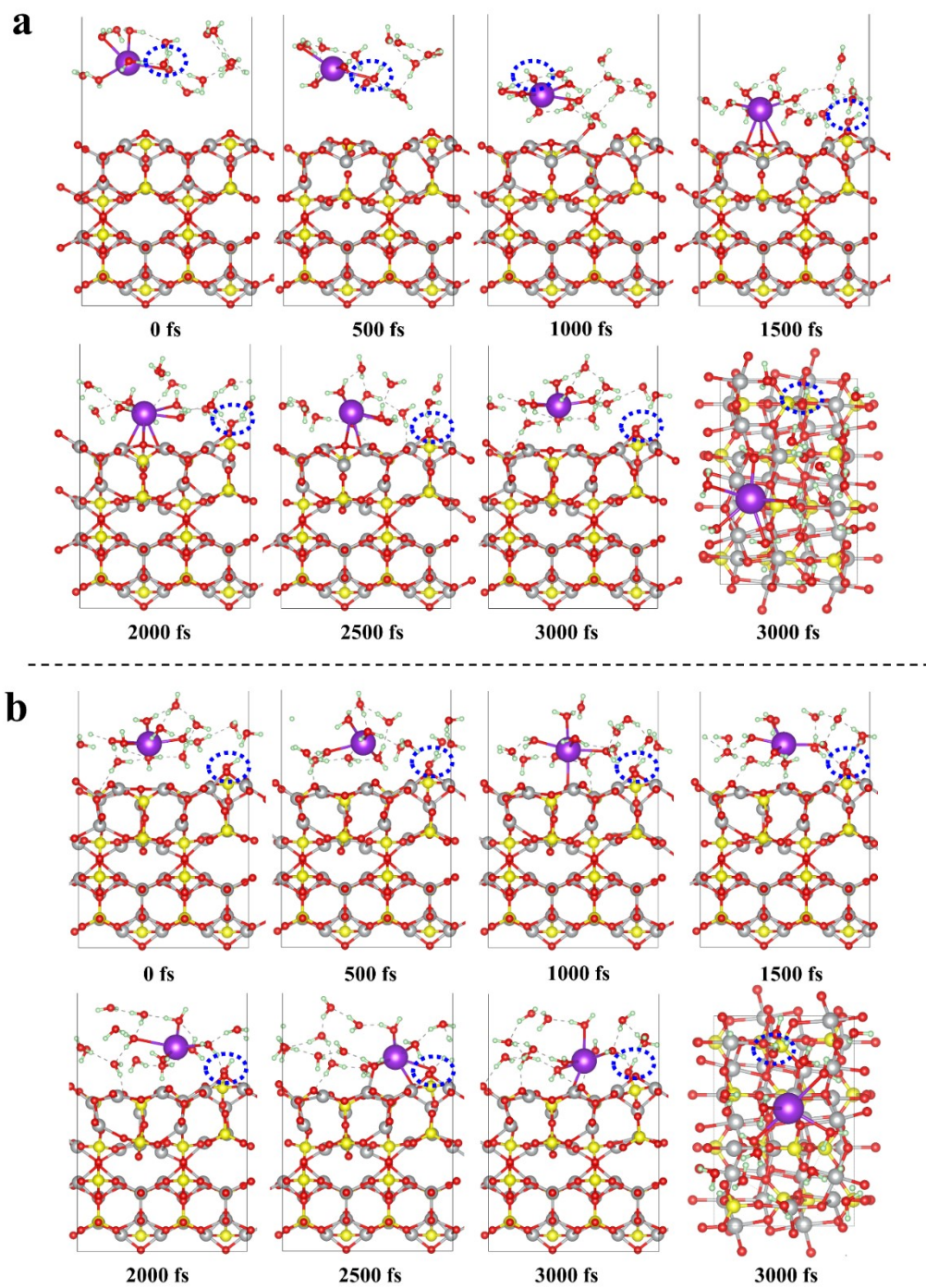
Fig. S15. a) NVT and b) NVE experiments of P-NiO with changing K$^+$ position.
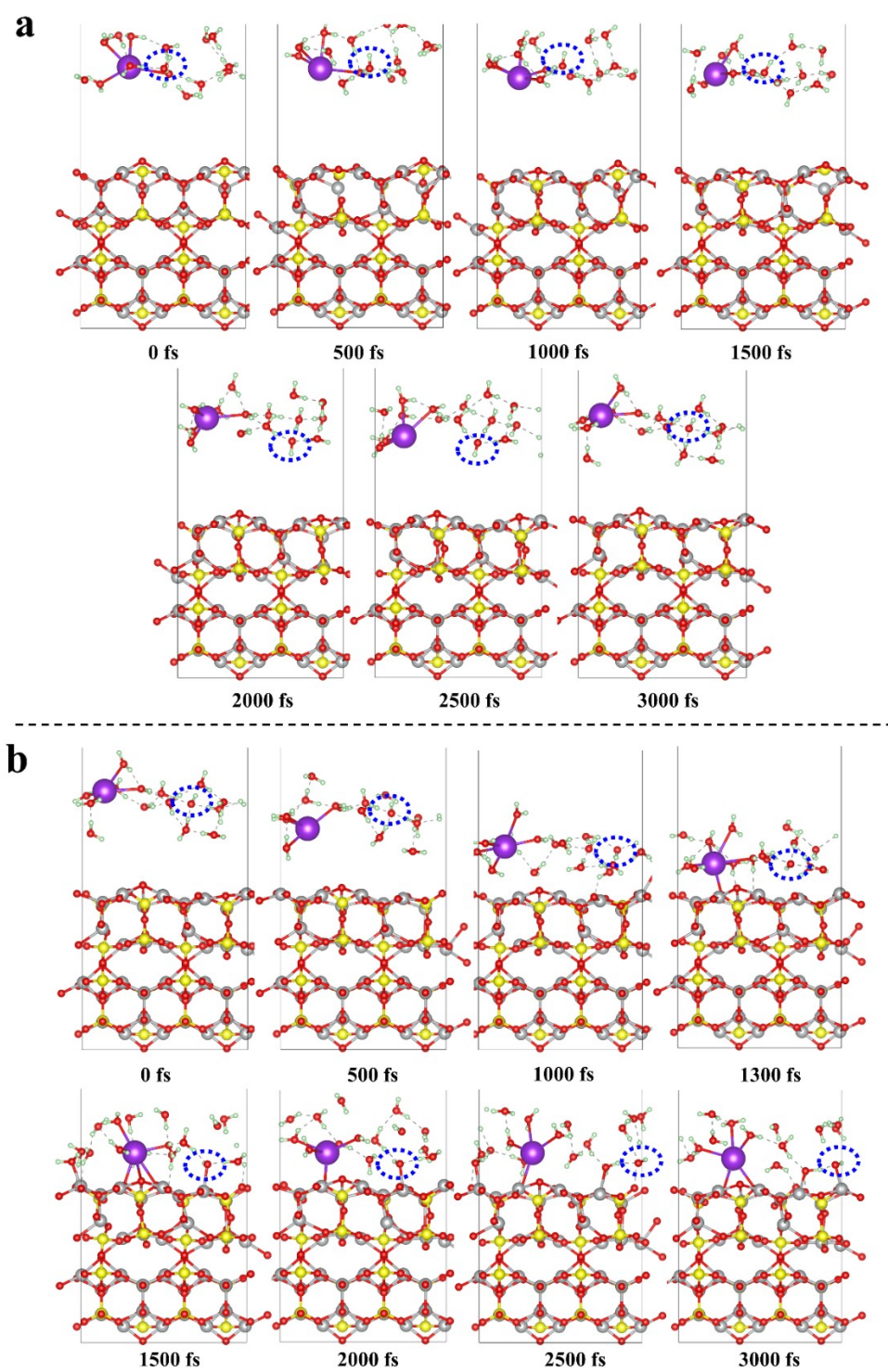
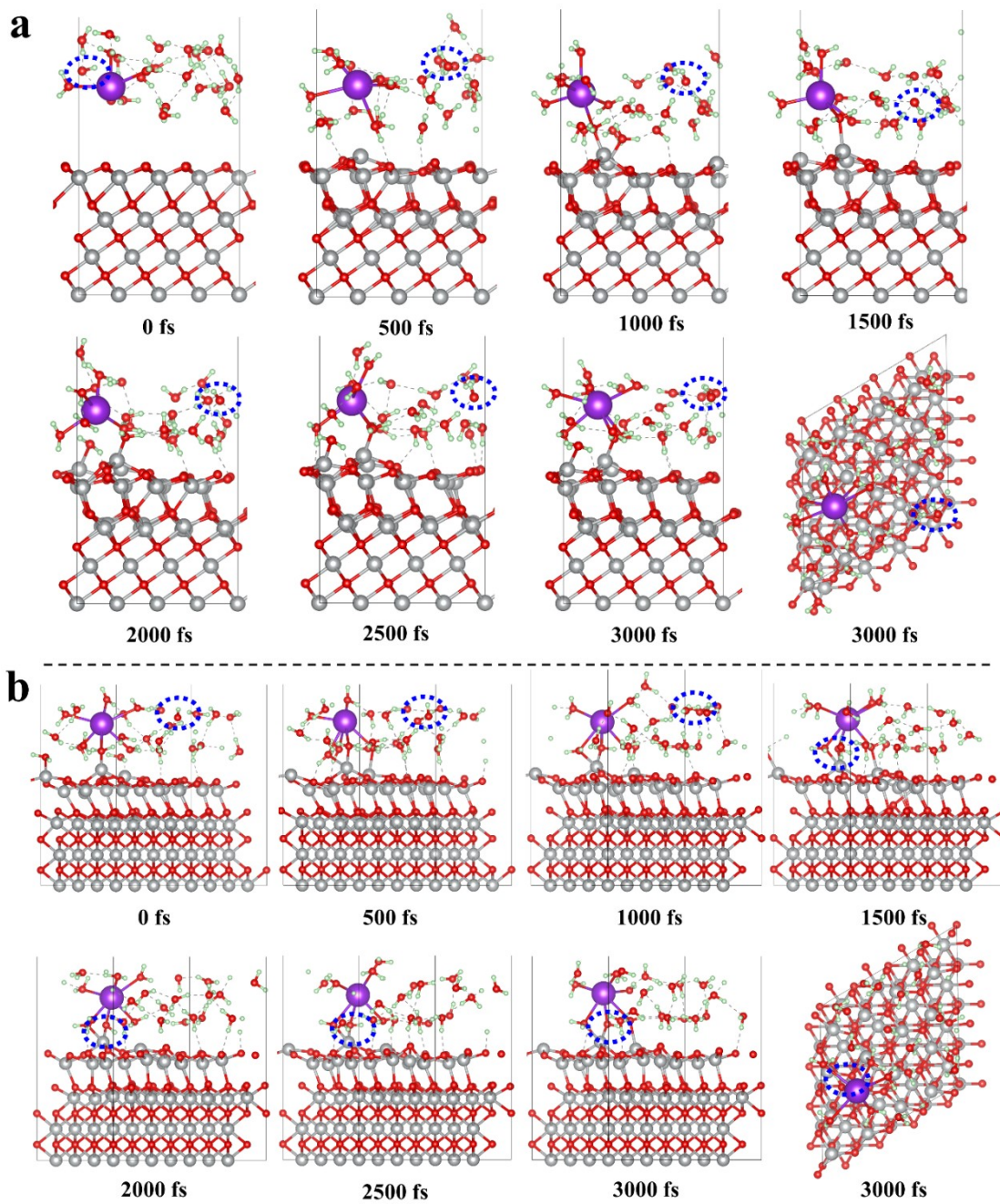**Fig. S16.** a) NVT and b) NVE experiments of P-NiO with increased adsorption distance.

Fig. S17. a) NVT and b) NVE experiments of NiO with changing K^+ position.
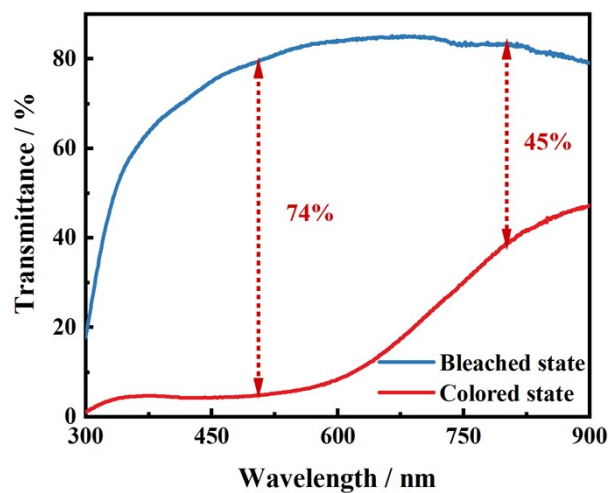
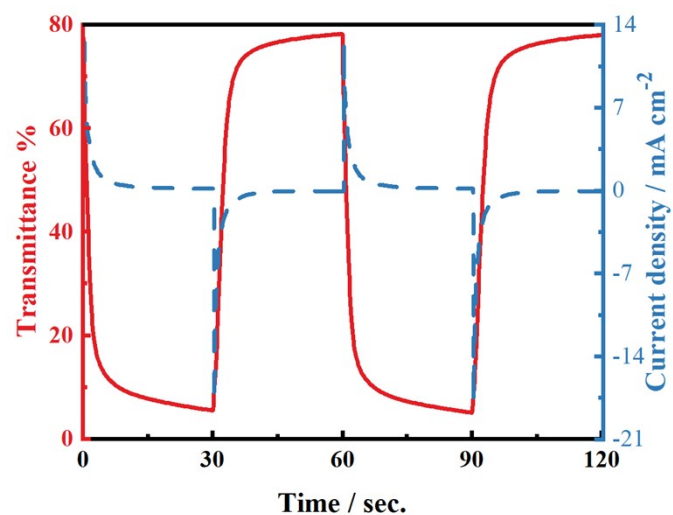**Fig. S18.** Spectral behavior of the device from 300 nm to 900 nm at −0.3 V and 1.2 V.

Fig. S19. Changes in the transmittance of the device with the applied potential of 0 V and 0.7 V for 30 s each at 500 nm.
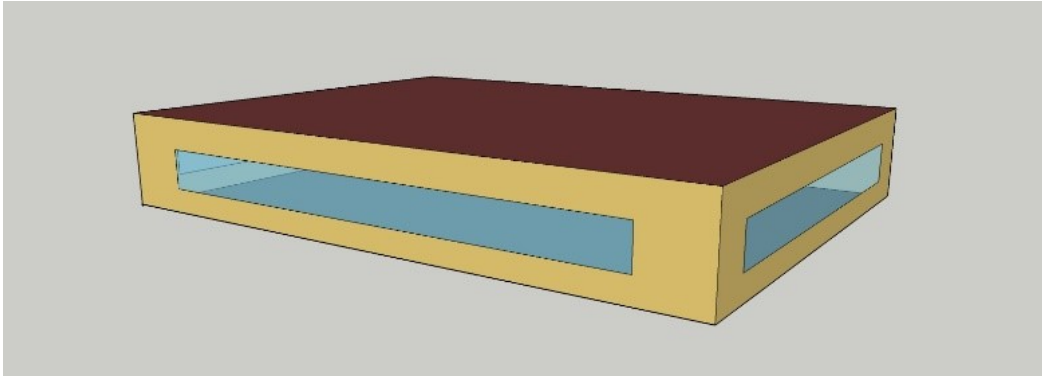
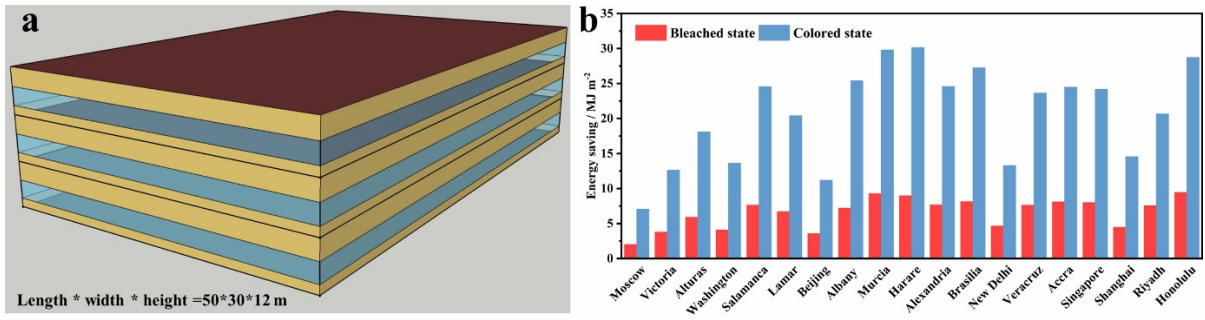**Fig. S20.** Geometrical model of a 15×10×3 m building for energy simulation.

Fig. S21. a) Geometrical model of a 50×30×12 m building for energy simulation. b) Predicted energy saving compared with a clear 3 mm window.

Table S1. Comparison of electrochromic performance of NiO-based electrochromic devices.

Device	T_b	ΔT (%)	t_b/t_c (s)	CE (cm^2 C^{-1})	References
NiO‖TiO$_2$	76	74	–	65.1	J. Phys. Chem. Lett., 2023, 14, 2284-2291
WO$_3$‖NiO	77	62	10/13.1	131.9	Nanoscale, 2016, 8, 348-357
AgNWs‖NiO	80	14.3	–	51.9	Adv. Energy Mater. 2018, 8, 1800069
NiO‖FTO	58	47	6.7/2.7	85.3	J Solid State Electrochem., 2021, 25, 821–830
WO$_3$‖NiO	75	46	3.1/4.6	90	Scientific Reports, 2020, 10, 8430
NiO‖Li$_4$Ti$_5$O$_{12}$	65	55	7.4/6.5		J. Mater. Chem. A, 2021, 9, 6451-6459
NiO‖MnO$_2$	78	57	12/12.1	28.5	J. Mater. Chem. C, 2021, 9, 14378-14387
NiO$_x$‖ITO	69	60	11.8/4	25.6	ACS Appl. Mater. Interfaces 2013, 5, 6502-6507
NiO‖TiO$_2$	81	80.3	34.8/34.2	31.7	Nanoscale, 2023, 15, 8685-8692
NiHPO$_4$	80	73.5	21.6/26.6	66.5	Nano-Micro Letters (2023),41-53.
P-NiO	**79**	**74.2**	**5.0/5.3**	**72.5**	**This work**

Table S2. Information of the building model.

Items	Specifications
Window locations	Even distribution among all four sides
Floor to ceiling height	3 m
Glazing sill height	0.76 m
Outer walls	Stucco/Concrete/Wall insulation/Gypsum
Interior walls	Gypsum board/Wall air space resistance/Gypsum board
Roof	Roof membrane/Roof insulation/Metal decking
Floor	Concrete/Carpet pad

Supplementary References

1 G. F. Cai, J. P. Tu, J. Zhang, Y.J. Mai, Y. Lu, C. D. Gu and X. l. Wang, *Nanoscale*, 2012, **4**, 5724-5730.

2 J. P. Perdew, K. Burke and M. Ernzerhof, *Phys. Rev. Lett.*, 1996, **77**, 3865.

3 J. VandeVondele, M. Krack, F. Mohamed, M. Parrinello, T. Chassaing and J. Hutter, *Comput. Phys. Commun.*, 2005, **167**, 103-128.

4 J. Hutter, M. Iannuzzi, F. Schiffmann and J. VandeVondele, *Wiley Interdiscip. Rev.: Comput. Mol. Sci.*, 2014, **4**, 15-25.

5 J. VandeVondele and J. Hutter, *J. Chem. Phys.*, 2007, **127**, 114105.

6 S. Goedecker, M. Teter and J. Hutter, *Phys. Rev. B*, 1996, **54**, 1703.

7 M. A. Carignano, A. Kachmar and J. r. Hutter, *J. Phys. Chem. C*, 2015, **119**, 8991-8997.

8 S. Grimme, *J. Comput. Chem.*, 2006, **27**, 1787-1799.

9 G. J. Martyna, M. L. Klein and M. Tuckerman, *J. Chem. Phys.*, 1992, **97**, 2635-2643.